Eur. Phys. J. A (2014) **50**: 8
DOI 10.1140/epja/i2014-14008-y

THE EUROPEAN PHYSICAL JOURNAL A

Regular Article – Experimental Physics

MINOS: A vertex tracker coupled to a thick liquid-hydrogen target for in-beam spectroscopy of exotic nuclei

A. Obertelli[1,a], A. Delbart[1], S. Anvar[1], L. Audirac[1], G. Authelet[1], H. Baba[2], B. Bruyneel[1], D. Calvet[1], F. Château[1], A. Corsi[1], P. Doornenbal[2], J.-M. Gheller[1], A. Giganon[1], C. Lahonde-Hamdoun[1], D. Leboeuf[1], D. Loiseau[1], A. Mohamed[1], J.-Ph. Mols[1], H. Otsu[2], C. Péron[1], A. Peyaud[1], E.C. Pollacco[1], G. Prono[1], J.-Y. Rousse[1], C. Santamaria[1], and T. Uesaka[2]

[1] CEA, Centre de Saclay, IRFU, F-91191 Gif-sur-Yvette, France
[2] RIKEN Nishina Center, 2-1 Hirosawa, Wako, Saitama 351-0198, Japan

Received: 28 October 2013 / Revised: 14 January 2014
Published online: 30 January 2014 –
Communicated by A. Alamanos

Abstract. MINOS is a new apparatus dedicated to in-beam nuclear structure experiments with low-intensity exotic beams in inverse kinematics at intermediate energies above 150 MeV/nucleon. The device is composed of a thick liquid-hydrogen target coupled to a compact time projection chamber (TPC) serving as a vertex tracker. Either used for in-beam gamma spectroscopy of bound excited states or invariant-mass spectroscopy of unbound states, MINOS aims at improving the luminosity by a very significant factor compared to standard solid-target material experiments while improving experimental resolutions.

1 Introduction

Atomic nuclei are few-body systems mainly governed by the strong force and quantum-mechanical laws. They are composed of nucleons interacting through the in-medium nuclear forces. Their structure is characterized by energy orbitals which can be filled by nucleons respecting the Pauli exclusion principle. The sequence of these single particle energies is highly non-homogeneous and consists of energy regions with a high density of orbitals (the energy shells) separated by large energy gaps. These gaps represent the backbone of nuclear structure and are a direct fingerprint of the nuclear interactions. The number of nucleons that define a closed shell (*i.e.* a shell completely filled with nucleons) is called magic. Magic numbers of nucleons are well established for stable nuclei: 2, 8, 20, 28, 50, 82, 126 but are known not to be universal over the nuclear chart. Indeed, the nuclear shell structure is known to change, sometimes drastically, with the number of protons and neutrons, revealing how delicate the arrangement of nucleons in interaction is. The study of unstable nuclei away from the valley of stability is the only possibility to establish the structure of nuclei throughout the nuclear chart and unravel the isospin properties of the nuclear shell structure as well as the in-medium nuclear forces. New shell closures or strong shell reordering are predicted in several regions at the limit or beyond the reach with current setups and beam intensities. For example, the $N = 20$ and $N = 28$ shell gaps are known to vanish for neutron-rich nuclei [1–3], the $Z = 28$ shell closure is claimed to weaken in the region of the doubly magic ^{78}Ni and subshell closures are under investigation at $N = 32, 34$ [4–6]. The three-body interaction has recently been demonstrated to be a very crucial ingredient to understand shell evolution with isospin and, for instance, to accurately reproduce the binding energies of neutron-rich oxygen isotopes and correctly predict the neutron dripline at ^{24}O [7], *i.e.* the last bound oxygen isotope with respect to the nuclear force. All these features originate in the properties of the in-medium nucleon-nucleon interaction and three-body forces [8,9].

Different observables, such as the ground-state binding energy or the excitation energy of the first excited state, can be used to characterize nuclear shell gaps. In-beam spectroscopy at intermediate energy using thick targets is one of the most efficient ways to investigate shell structure properties far from stability. Unfortunately, the most exotic species and many physics cases of prior importance are not reachable with the currently employed experimental techniques and the very low production intensities for these nuclei. In the following, we focus on a new setup dedicated to experiments that reconstruct such observables from the decay particles and/or photons produced after nucleon knockout reactions. We can divide these reactions into two types: i) in-beam γ spectroscopy of the fragment nucleus produced in a bound excited state, ii) in-beam invariant mass spectroscopy of the fragment nucleus

[a] e-mail: alexandre.obertelli@cea.fr

produced in a particle-unbound excited state. The emitted particle, when dealing with neutron-rich nuclei is mostly one or several neutrons.

In even-even nuclei, the excitation energy of the first excited 2^+ state, in most cases the first excited state, is very sensitive to the shell structure above the Fermi level. Experimentally, the spectroscopy of the most exotic isotopes has been reached, in many cases, via prompt γ spectroscopy from secondary reactions of exotic beams produced by fragmentation at intermediate energies. The excitation energy of the first excited state in even-even nuclei is a measurement of the orbit density above the Fermi level: magic nuclei's first excited state presents a large excitation energy intimately linked to the considered energy gap. Worldwide, four laboratories are using this technique (GANIL in France, GSI in Germany, NSCL in USA and RIKEN in Japan) and have recently provided, for instance, the first spectroscopy of ^{42}Si [3], ^{32}Ne [10] or ^{54}Ca [6], all leading to new and crucial experimental information concerning shell structure or shape evolution with isospin. Among these laboratories, the future FAIR facility in Europe and the new Radioactive Ion Beam Facility (RIBF) at RIKEN in Japan will share in the next 10 years the leadership in producing very exotic nuclei at energies above 150 MeV/nucleon. Nucleon knockout reactions have indeed demonstrated to be very efficient in populating the most exotic species and to perform their prompt γ-decay spectroscopy when bound states are populated or their invariant-mass spectroscopy for states above the nucleon separation threshold.

In the case of short-lived and bound-state spectroscopy, this method is based on the coupling of a γ spectrometer (Germanium or scintillator arrays) around a heavy-ion target, usually ^{12}C or ^{9}Be, and an identification device for the projectile-like fragment. The γ-rays are detected in coincidence with the knockout residue and identified in mass and atomic number by the a recoil detector. The measured energy E_γ is corrected from the Doppler shift due to in-flight emission, following the relation

$$E_0 = E_\gamma \frac{1-\beta\cos(\theta)}{\sqrt{1-\beta^2}}, \quad (1)$$

where E_0 is the nuclear transition energy in the nucleus frame, β is the velocity of the projectile-like fragment when the transition is emitted and θ is the angle defined by the ejectile velocity and the emitted γ-ray direction.

The power of a γ-ray detection setup for intermediate-energy studies, in addition to its geometrical efficiency, is directly related to its capability to perform a good Doppler correction. This depends on i) the angle of the photon relative to the scattering angle of the residue which is strongly related to the γ-ray detector granularity, and ii) the velocity of the ejectile when emitting the photon. This last point, is related for prompt decays to the energy loss of the beam and the resulting velocity spread inside the target.

For a given beam intensity, all existing setups are therefore limited by the same parameters: i) The energy- and position-resolution and efficiency characteristics of the γ spectrometer. This limitation will be soon largely reduced by new-generation high-resolution $4\,\pi\,\gamma$ arrays, such as the European AGATA spectrometer [11] with a ~ 4 mm position resolution for the first-interaction position. Compared to existing arrays, the gain in sensitivity with AGATA can reach 20 in case of low-multiplicity intermediate-energy studies. ii) The choice of the target is a compromise between a thick target to increase the statistics and a thin target to increase the sensitivity of the detection by minimizing the energy loss, and therefore the velocity spread, in the target and for a better Doppler-effect correction. Indeed, up to now in prompt γ spectroscopy, one does not have access to the velocity of the fragment when it emits the photon from inside the target.

In the case of invariant-mass measurements of unbound states of neutron-rich nuclei, excitation energies above the neutron(s) separation energy of the final state are obtained from the exclusive measurement of quadrivector momenta of decaying residues (projectile like and in-flight emitted neutrons), following the relation:

$$E_{rel} = \sqrt{\left(\sum_i T_i\right)^2 - \left(\sum_i \overrightarrow{p_i}c\right)^2} - c^2 \times \sum_i M_i, \quad (2)$$

where T_i, $\overrightarrow{p_i}c$ and M_ic^2 are the kinetic energy, momentum and mass of the residues. As in prompt γ spectroscopy, the target thickness is a limiting factor to the resolution through the impact of energy loss and straggling in the measurement of momenta (both kinetic energies and scattering angles).

We developed MINOS[1], a new technique to use nucleon-removal from very exotic nuclei on a very thick liquid-hydrogen target coupled to a proton tracker that aims at measuring the reaction-vertex position in the target on an event-by-event basis. The concept of MINOS has already been introduced in [12,13]. The main part of the detection system is based on a Time Projection Chamber (see [14,15] for a recent example of application of a TPC in low-energy nuclear physics). A scheme of the proposed design is shown in fig. 1. By measuring this vertex, one allows for the use of targets of hundreds of millimeters with improved detection sensitivity, *i.e.* the Doppler correction is better than with a passive heavy-ion target. The only remaining limiting factor is that one has to ensure that the second-interaction probability in the target is low since the knockout fragment has to be identified after the target. For incident energies of 200–400 MeV/nucleon, a typical length of 150 mm allows to fulfill this condition. This development will induce a unique gain in detection sensitivity of more than one order of magnitude compared to experiments with solid heavy-ion targets. When used with the new generation AGATA array, the gain will amount to about several hundreds compared to existing setups, allowing a detailed spectroscopy of nuclei produced at less than 1 particle per second and leading to the potential discovery of new shell effects further inside the Terra Incognita of the nuclear landscape.

[1] Quasi-acronym for "nuclear MagIc Numbers Off Stability".

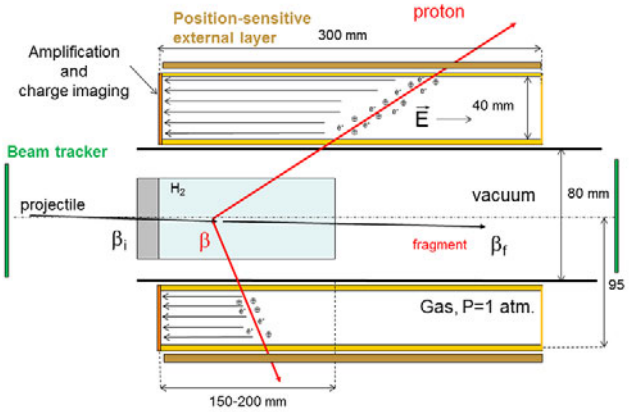

Fig. 1. (Color online) Principle scheme of the MINOS device. Reactions with at least one recoil proton emitted with significant momentum transfer in the exit channel such as $(p, 2p)$ and (p, pn) represent the core program of MINOS.

In this article, we present details of the MINOS device. Simulation-based specifications for such a device are discussed in sect. 2. A brief overview of the system is given in sect. 3 followed by a detailed description of the different subparts of MINOS: the target (sect. 4), the TPC and external layer (sect. 5), the electronics (sect. 6) and data acquisition system (sect. 7). Finally, very first cosmic-ray data will be shown to demonstrate that MINOS is now in working conditions (sect. 8). Detailed studies of the detector performances with cosmic ray and in-beam tests have been performed and are the object of a future publication.

2 Specifications

To achieve the optimum energy resolution, a reaction vertex resolution of 3 mm FWHM has to be achieved. The efficiency to reconstruct a $(p, 2p)$ vertex should be larger than 80% in order to reach an effective design. These two features represent the specifications of MINOS.

The characteristics of the MINOS device to fulfill the above requirements, including detector and target geometry, detector granularity and gas composition were derived from Monte Carlo simulations and are discussed in the following.

2.1 Monte Carlo simulation description

Simulations are performed in three consecutive steps: i) a GEANT4 [16] simulation including a reaction process to generate events and tracking particles in the device, ii) a Monte Carlo simulation for the drift of ionization electrons in the TPC towards the amplification plane and for the amplification process including signal formation and electronics effects, iii) the reconstruction of the vertex position and the determination of the resolution via reconstruction algorithms.

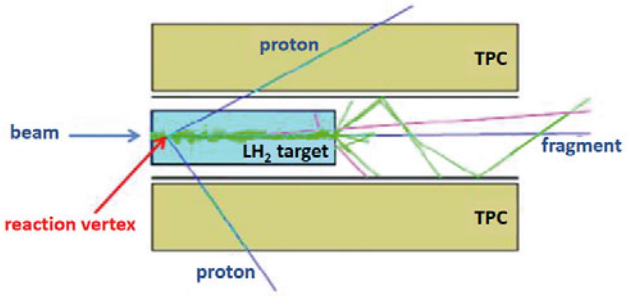

Fig. 2. (Color online) Example of a $(p, 2p)$ event from ^{53}K at 250 MeV/nucleon incident energy as obtained from the GEANT4 simulation. The reaction vertex is located just after the entrance of the target. The blue lines represent positive-charged particles: the heavy nuclei and protons which cross over the TPC. Electrons created along the proton and heavy-nuclei tracks appear in green whereas photons are shown in pink.

2.1.1 Track generation

Reactions in the target can be simulated using different reaction mechanism models. For MINOS, we used two different models. The reaction code INCL/ABLA [17,18], included in the GEANT4 package, allows to generate spallation fragments produced from the interaction of an heavy-ion and a proton from the proton target. This model is semi microscopic and gives the correct order of magnitude for the production rates of few nucleon removal [19, 20]. Reactions of interest can be selected for the following steps of the simulation. When dealing with a specific one-nucleon removal channel, such as $(p, 2p)$, the microscopic distorted-wave impulse approximation (DWIA) code Threedee [21] is used. In this case, the kinematics of protons from the reaction are directly implemented in the generator of protons in terms of angle and energy of emission.

When a reaction occurs at a given vertex position, particles are emitted. The evolution of particles is treated by the GEANT4 code. This first step allows to calculate the energy loss by the particles in the different volumes of the device. The interaction points along the track and the corresponding energy losses in the TPC active volume (gas) are recorded for the next step of the simulation. Figure 2 shows a $(p, 2p)$ event generated in GEANT4.

2.1.2 Drift of ionization electrons

The second step of the simulations consists of the drift of ionization electrons produced by charged particles in the gas of the TPC towards the detection plane. First, at each interaction point along the simulated track the number of primary ionization electrons N_e is calculated from the ratio $N_e = \frac{\Delta E}{I}$, where ΔE and I are the energy loss and the mean energy for the creation of a pair electron-ion in the considered gas. This number of primary ionization electrons is randomly generated following a Gaussian distribution centered in N_e with a deviation $\sigma = \sqrt{FN_e}$,

where F is the Fano factor taken as 0.2 in the following simulations with Ar-based gas mixtures [22].

The position (x, y) of each ionization electron after a drift time t is randomized from the position of creation (x_0, y_0, z_0), taking into account the drift velocity and transverse as well as longitudinal diffusions in the gas. Equation (3) gives this probability distribution for x and y coordinates defining the plane of pads perpendicular to the electric field and eq. (4) gives the distribution for the third dimension z where $\sigma_{T/L} = C_{T/L}\sqrt{z_0(\mathrm{cm})}$ with $C_{T/L}$ being the transverse/longitudinal diffusion coefficients of the gas. In these simulations, a homogeneous and constant electric field is considered in the TPC:

$$P_x(x_0;\sigma_T) = \frac{1}{\sqrt{2\pi}\sigma_T}\exp\left(\frac{-(x-x_0)^2}{2\sigma_T^2}\right), \quad (3)$$

$$P_z(z_0;\sigma_L) = \frac{1}{\sqrt{2\pi}\sigma_L}\exp\left(\frac{-(z-z_0)^2}{2\sigma_L^2}\right). \quad (4)$$

Diffusion coefficients σ_L, σ_T, and the drift velocity are taken from data tables accordingly to the conditions (gas mixture, voltage, pressure) considered for the simulation.

The position-sensitive detector is taken into account, in terms of its pad geometry and amplification stage of the ionization electrons. For each pad, a random gain G_i following a Polya distribution [22] given in eq. (5) is considered. This function depends on the average gain $\bar{G}$ and a scale parameter θ set to the typical value of 1 in the simulations,

$$P_G(G/\bar{G};\theta) = \frac{(\theta+1)^{\theta+1}}{\Gamma(\theta+1)}\left(\frac{G}{\bar{G}}\right)^{\theta}\exp\left(-(\theta+1)\left(\frac{G}{\bar{G}}\right)\right), \quad (5)$$

where Γ is the Gamma function.

The signal as a function of time $N(t)$ for each pad, given in eq. (6), is the sum, over the N primary electrons reaching this pad, after the Micromegas amplification and considering the response function of the electronics following the relation

$$N(t) \propto \sum_{i=1}^{N} G_i * \exp\left(-3\frac{t-t_i}{\tau}\right)\sin\left(\frac{t-t_i}{\tau}\right)\left(\frac{t-t_i}{\tau}\right)^3. \quad (6)$$

In this equation, $t_i = \frac{z_i}{v_d}$ is the time of creation of the electron which is obtained from the z_i coordinate and the drift speed of electrons in the gas v_d, and τ is the shaping time of the electronics. Finally, the signal is sampled in time and a white noise is added to each sample.

2.1.3 Reconstruction of tracks

The last step of the simulation is the reconstruction of the tracks. A threshold is applied to select pads for which the signal-over-noise ratio is larger than 5 times the $\sigma_{\mathrm{r.m.s.}}$ of the noise, similar to typical thresholds applied in physics experiments to avoid random triggering. The signal is analyzed by a mathematical function given in eq. (7), where

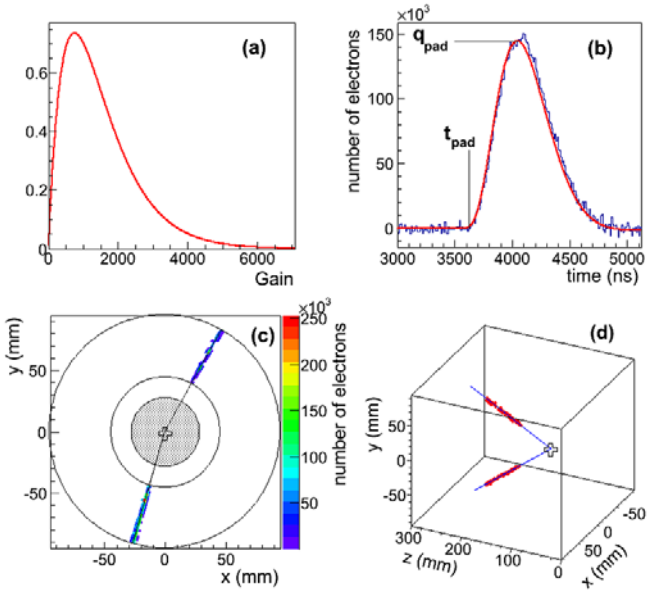

Fig. 3. (Color online) (a) Polya distribution of the gain with $G = 1500$ and $\theta = 1$ (see eq. (5)). (b) Pad signal waveform as a function of time. The time trigger t_{pad} and the number of electrons collected q_{pad} are extracted. (c) Number of electrons collected on the detection matrix ((XY) plane) after the drift for a $(p, 2p)$ reaction event. The vertex of reaction (cross), the projected trajectories of protons (lines), the target (gray circle) and the limits of the TPC (circles) are shown. (d) Final reconstruction in the three-dimension space of the trajectories of the protons for a $(p, 2p)$ event. The vertex (cross) is determined from the fit (blue lines) of the charges deposited by the protons in the TPC (red histogram).

Q_{pad} represents the total number of electrons collected on the pad (corresponding to the maximum of the fit) and t_{pad} is the trigger time of the pad converted in a drift distance z_0. Fitting all the pads that triggered gives a set of points (x_{pad}, y_{pad}, z_{pad}) weighted by a ponderation factor Q_{pad} proportional to the charge collected on the pad,

$$f(t) \propto Q_{pad} * \exp\left(-3\frac{t-t_{pad}}{\tau}\right)\sin\left(\frac{t-t_{pad}}{\tau}\right)\left(\frac{t-t_{pad}}{\tau}\right)^3. \quad (7)$$

The set of points are fitted by a parametrized function in the three-dimensional space, describing one or two parametric lines with the same vertex if one or two protons are detected.

Figure 3 illustrates several aspects of the simulation described above: the gain function, the analysis of the pad signal, the determination of the energy deposited on the detection plane and the vertex determination in the 3D space.

Moreover, the reconstruction of the vertex can be accessed with the reconstruction track of the beam before and after the target. For this purpose, silicon detectors are added, situated in the simulations 1300 mm upstream the target entrance window and 200 mm downstream the target exit window. A typical resolution of 1 mm at FWHM is considered for these detectors.

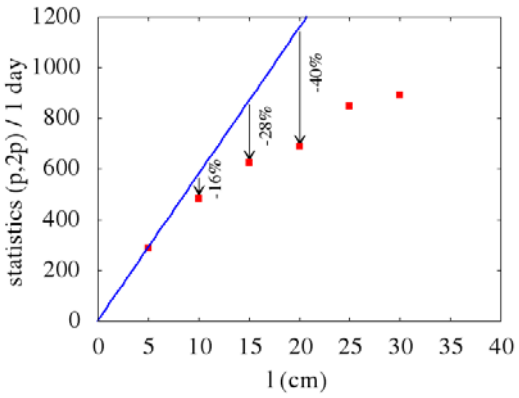

Fig. 4. (Color online) One-day statistics from ^{53}K$(p, 2p)$ for at 250 MeV/u kinetic energy impinging on a LH_2 target are plotted as a function of different target thicknesses. A 1 pps secondary beam intensity is considered. The statistics consider events for which only one reaction occurred. Non linearity as a function of the target thickness originates from multiple interactions in the target.

2.2 Results

Several combinations of gas, TPC dimensions, pad size and geometry have been investigated. In the following, we present the most important conclusions and their impact on the design and technical choices.

2.2.1 Target thickness

The optimum target thickness maximizes the $(p, 2p)$ reaction rate with exclusively one reaction in the target. The re-interaction probability, when the target is very thick, can be significant. To evaluate the amount of multiple reactions and to decide the optimum target thickness, a realistic reaction mechanism simulation has been used, namely the GEANT4 simulation including the INCL v5.1.14 physics list. The $(p, 2p)$ channel has been tagged by selecting events for which the projectile-like fragment has $A = A_{beam} - 1$ and $Z = Z_{beam} - 1$ and two protons are ejected. The results are shown in fig. 4 as a function of different target thicknesses for a typical reaction of interest, namely ^{53}K$(p, 2p)$ at 250 MeV/nucleon. In this specific case, the rate of $(p, 2p)$ reactions increases almost linearly up to 100 mm, and then saturates at 200–300 mm. This saturation can be understood as an increased probability of having further interactions of the projectile with the target, depleting the $(p, 2p)$ channel. With the identification of $(p, 2p)$ residues downstream the MINOS device, one-reaction events only can be selected and multiple-reaction events can be filtered out.

Interestingly, the analytic solution of the problem yields an optimum thickness $\ell = 1/(\sigma_R \rho)$, where σ_R is the total reaction cross section and ρ is the target density. For liquid hydrogen and a reaction cross section of 1 barn, this yields $\ell = 230$ mm.

Eventually, another considerations will play a role in the choice of the target thickness. The beam tracking and the measurement of the projectile-like momentum distribution downstream the target will be affected by angular straggling in the target. Also, the higher the total kinetic energy, the better the acceptance and resolution of the spectrometer will be. Energy loss and straggling in different target thicknesses for the reaction shown in fig. 4 are listed in table 1. Taking into account all the factors discussed above, we conclude that the optimum thickness is in the 150–200 mm range from medium- to light-mass nuclei.

Table 1. LH_2 target thickness and corresponding energy loss and angular straggling of a ^{53}K beam at 250 MeV/u kinetic energy.

Thickness (mm)	E_{loss} (MeV)	σ_θ (mrad FWHM)
150	65	1.2
200	90	1.5
250	118	1.7
300	150	1.7

2.2.2 Target and TPC geometry

Three main results are retained: i) The largest contribution to the position resolution of the reaction vertex comes from the angular straggling in the target and materials surrounding it. ii) The closer to the target the inner ring of the detection plane of the TPC is, the better is the resolution. This means that a compact geometry is preferred. iii) The geometry of the pads does not have a significant role on the resolution once the mean area of one pad does not exceed 4 mm^2. Too small pads will increase the number of channels and lead to a degraded signal-over-noise ratio.

Concerning the TPC length, it is chosen to maximize the detection efficiency of protons from $(p, 2p)$ reactions. For the Micromegas, a concentric matrix of 18 rings divided into 256 pads was chosen, leading to 4608 electronics channels for the TPC.

Typical efficiency for a 300 mm long TPC and a 150 mm long and 56 mm wide target is about 80–90% for at least one proton detected depending on the considered $(p, 2p)$ reaction.The 10–20% loss corresponds to events with very asymmetric angles for the two protons: one is emitted at low energy at large angle and does not exit the target and the second proton is emitted at high energy in the beam direction, outside the TPC geometrical acceptance. Typically, protons emitted below 30 MeV in the $(p, 2p)$ reaction do not enter the TPC since the range of a 30 MeV proton in solid hydrogen is estimated to be 55 mm. Details on the simulated angular acceptance for the ^{53}K$(p, 2p)$ reaction at 250 MeV/nucleon is illustrated in fig. 5.

Although the primary goal of MINOS is a vertex tracker and the extraction of inclusive one-nucleon removal cross sections with no specific distinction of the

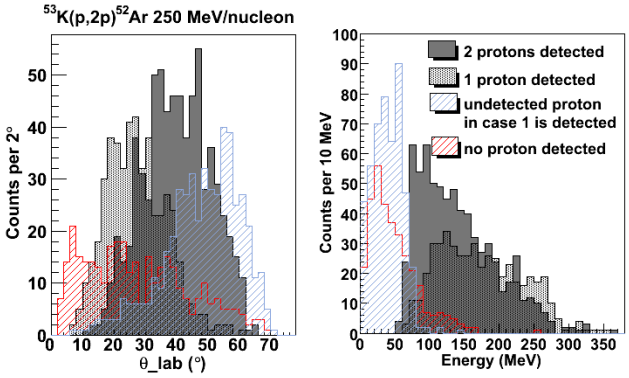

Fig. 5. (Color online) Realistic simulation for the kinematics of protons from the reaction $^{53}\mathrm{K}(p,2p)^{52}\mathrm{Ar}$ at 250 MeV/nucleon. The reaction process is simulated with the INCL4 intra-nuclear cascade code [17,18]. Events for which both protons are detected (gray) or only one proton (black dots) are shown. The kinematics of missed protons are also shown in the case both protons (red) or only one proton (blue) are missing.

reaction mechanism, the extraction of reliable spectroscopic factor by comparison to theoretical single-particle cross sections, could be much cleaner if exclusive distributions are compared to theory. For example, the restriction to scattering angles around 45 degrees (large momentum transfer) and a selection on the relative scattering angle between the two protons can be a good way to maximize the contribution to direct processes and a proper structure information extraction from the data. It may not be as perfect as a full exclusive measurement with missing mass but much cleaner than what can be done with inclusive heavy-ion collisions. These differential distributions can be extracted if statistics allow it. In this case, the overall detection efficiency for detecting two protons has been simulated to be 50% in the case of fig. 5 and fig. 6. The reconstruction efficiency of these events with the current algorithms has been tested to be close to 100% from simulated events.

2.2.3 Gas choice

The gas for the TPC is a trade-off between electron transverse and longitudinal diffusions, electron drift speed and gain in the Micromegas amplification gap. Argon is chosen for its low average energy required to produce one ion/electron pair (26 eV). CF_4 is used to speed up the electron drift velocity and lower the diffusions in the 200–300 V/cm electric field range. Isobutane (i-C_4H_{10}) is chosen for its known quencher capabilities for the amplification avalanche process required at the anode side of the TPC where the segmented detection plane is to be placed. The proportions of isobutane and CF_4 are defined from Magboltz [23] simulations and gain measurements performed with a 128 μm gap bulk-micromegas prototype (see sect. 5.2). A non-flammable mixture of argon, CF_4 and isobutane, respectively with the proportions 82%, 15% and 3%, is retained as a baseline candidate. The typical values used in the simulations are listed in table 2 for an electric field of 300 V/cm corresponding to a high voltage for the cathode of 9 kV.

Table 2. Parameters used for the MINOS simulations: geometrical characteristics of the liquid-hydrogen target and the TPC, features of the gas for an electric field of 300 V/cm, characteristics of the electronics used in the simulation, noise and detection threshold.

Dimensions	
Target length	150 mm
Target radius	28 mm
TPC length	300 mm
TPC inner radius	45 mm
TPC outer radius	55 mm
Gas	
Composition	$Ar_{82}(CF_4)_{15}(iso)_3$
Longitudinal diffusion	186 $\mu m/\sqrt{cm}$
Transverse diffusion	195 $\mu m/\sqrt{cm}$
Drift speed	66 μm/ns
Ionisation threshold	26 eV
Average gain	1500
Electronics	
Shaping time	426 ns
Time sampling	10 ns
Noise ($\sigma_{\mathrm{r.m.s.}}$)	2500 electrons r.m.s.
Detection threshold	$5\sigma_{\mathrm{r.m.s.}}$

2.2.4 Electronics requirements

The simulations performed allow to verify that digital electronics with 100 MHz sampling frequency and noise of the order of 2500 electrons is suitable to achieve the requirements with the proposed experimental device. Tracks of protons around 100 MeV have to be reconstructed in three dimensions. Questions of signal-over-noise ratio and time resolution are of prior importance relatively to i) the low energy loss by protons in the TPC (typically 20 keV for high energy protons), ii) the noise around 2500 electrons r.m.s. essentially due to the length of cables, and iii) the determination of the arrival time of primary electrons on the pads.

The parameters used in the simulations to shape and sample the electronic signal are listed in table 2. A detection threshold of $5\sigma_{\mathrm{r.m.s.}}$ of the noise is suitable to select the proton signals and eliminate pads triggering on the noise. Indeed, a simple estimate gives about 20 primary electrons per pad, yielding around 28000 electrons after amplification compared to the 12500 electrons corresponding to $5\sigma_{\mathrm{r.m.s.}}$ of the noise. This last value is equivalent to the signal of a proton losing 15 keV per track.

2.2.5 Resolutions

The vertex resolution is calculated for two typical candidate physics cases with the MINOS setup: ^{54}Ca and ^{53}K at

Table 3. Reconstruction resolution (FWHM) obtained over the vertex of emission for ^{53}K and ^{54}Ca interacting by $(p, 2p)$ and (p, pn) reactions respectively at 250 MeV/nucleon. Two examples of $(p, 2p)$ and (p, pn) reactions with different kinematics are shown. In the analysis of simulated tracks, a simple linear fit of the tracks has been used.

	INCL-ABLA	Threedee
^{53}K$(p, 2p)$	2.6 mm	4.0 mm
^{54}Ca(p, pn)	4.3 mm	5.8 mm

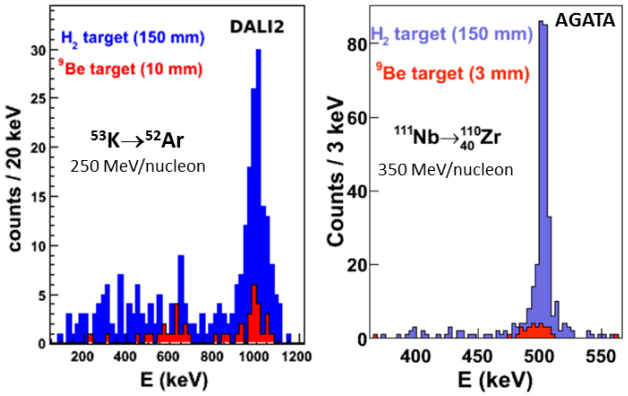

Fig. 6. (Color online) Left: Simulation of a Doppler corrected γ spectra from the in-flight decay of ^{52}Ar produced via $(p, 2p)$ at an incident energy of 250 MeV/nucleon. The spectrum obtained with MINOS and with a 10 mm thick Be target are compared. In the simulations, the DALI2 scintillator array is considered. Right: Simulations of a Doppler corrected γ-ray spectrum from the in-flight decay of ^{111}Nb produced via $(p, 2p)$ at incident energy of 350 MeV/nucleon. The spectra obtained with MINOS and with a 3 mm thick Be target are compared. In the simulations, 10 triple clusters of the AGATA array are considered. All transitions are assumed to be prompt (no γ-ray decay half-lives).

250 MeV/nucleon reacting through (p, pn) and $(p, 2p)$ reactions, respectively. Using the beam tracking reconstruction plus one proton detected in the TPC allows for a better determination of the vertex than using only the two proton tracks for $(p, 2p)$ reactions when both protons are detected. Indeed, for a significant part of the events, one of the two proton has a kinematics that lead to a degraded resolution whereas the other one offers a better kinematics in view of tracking the vertex.

Resolutions obtained are listed in table 3 and vary between 2.6 and 5.8 mm according to the reaction considered and the kinematics used for two 1 mm FWHM resolution beam tracking detectors positioned at 1300 mm upstream and 200 mm downstream the hydrogen target. Concerning the time resolution, typical values better than 20 ns are found at FWHM, leading to a spatial resolution along the drift field of about 1 mm.

In the present analysis, we employ simple parametric lines to fit trajectories of particles. In the future, more complex algorithms could be used in order to reach a better efficiency and quality of vertex reconstruction.

As an illustration of the gain in sensitivity expected in upcoming experiments, a complete simulation of a γ-ray spectrum measured with the DALI2 scintillator array [24] and MINOS (150 mm thick hydrogen target) for a 1 MeV transition emitted in flight by ^{52}Ar produced by the ^{53}K$(p, 2p)$ reaction at 250 MeV/nucleon is illustrated in the left panel of fig. 6. Note that the gain in resolution is limited here by the intrinsic energy resolution of the NaI scintillators and the angular resolution limited by the size of the DALI2 detectors. A gain of 5 in statistics is expected. Note that MINOS, not illustrated in this picture, will also offer the possibility to measure parallel momentum distributions with a resolution expected to be of the order of 100–150 MeV/c, sufficient to get information on the intrinsic angular momentum of the removed nucleon. Such information usually cannot be accessed with thick targets. The right hand side of fig. 6 illustrates a similar comparison for the reaction ^{111}Nb$(p, 2p)^{110}$Zr at 350 MeV/nucleon but with use of ten Ge triple clusters of the new generation AGATA array. The high resolution and granularity of such a γ array will allow a full exploitation of the capabilities of MINOS, and *vice versa*.

3 Overview and setup at RIKEN

The above-mentioned simulations allowed to converge on a compact design for the MINOS ensemble. The mechanical support of the device and the location of the electronics have been mainly guided by the environment for which the detector has been designed to be used first at the RIBF at RIKEN, either at SAMURAI [25] or at the Zero-Degree Spectrometer [26] focal point. A significant part of the foreseen experiments is based on a combined use of the DALI2 scintillator array [24] and MINOS. A 3D CAD drawing of the TPC inside the DALI2 array at the F8 focal point of the BigRIPS separator [26] is shown in fig. 7. The full system (target, TPC and electronics) can be mounted on its frame separately from the beam line and DALI2. The support has been conceived in such a way that it can be combined with DALI2 and removed in one step from the top, as a whole. An advantage of this configuration is the location of the electronics and cooling system, placed upstream the target, leading to a compact geometry and an optimal coupling to DALI2. As ancillary detectors, 300 μm thick silicon-stripped detectors are available to be placed at the entrance and exit of the reaction chamber of the MINOS target. An extra position-sensitive layer surrounding the TPC has also been conceived for i) potential use as a trigger and ii) drift velocity calibration of physics events during the measurement (see sect. 5.4).

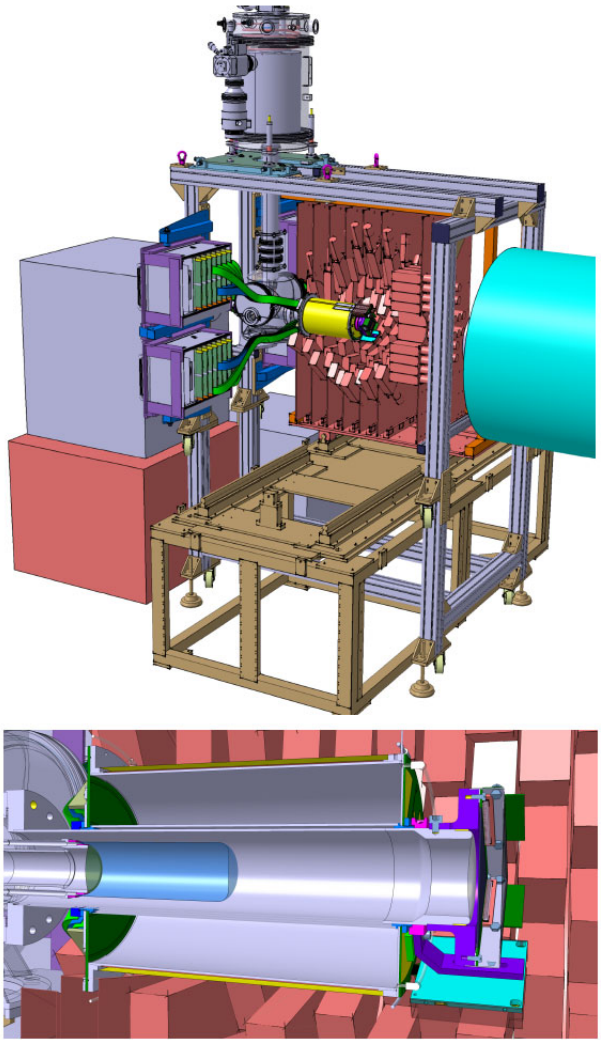

Fig. 7. (Color online) 3D drawing of the MINOS device inserted inside the DALI2 array (red). The TPC (yellow), the target (blue), the readout electronics and the signal cables (green) are shown. Top: General view. Bottom: Zoom on the target-TPC system. See text for details on these different parts.

4 Hydrogen target

The Magnetism and Cryogenics laboratory (SACM) of CEA-IRFU developed several liquid targets for different experiments or projects such as Polder at Jefferson Lab in 1996 or the PRESPEC Collaboration at GSI in 2011 [27] and thin solid targets [28]. The MINOS target design is similar to the one described in [27]. The adopted cryogenic design minimizes the amount of hydrogen in the system. A cryo-cooler is used for the liquefaction of the gas, simplifying the installation in any laboratory with no need of helium supply in the experimental area. A front view of the target during the filling phase is shown in fig. 8.

The system consists of two parts: i) the cold part composed of the cryostat and the liquid target located in the experimental area, ii) the control-command and warm hydrogen gas section. This second part of the system is composed of two distinct racks. The control-command is used to pilot and watch the installation and the cryo-rack allows a safe hydrogen transfer to the target. At the end of operation the full volume of hydrogen is transfered to the initial tank.

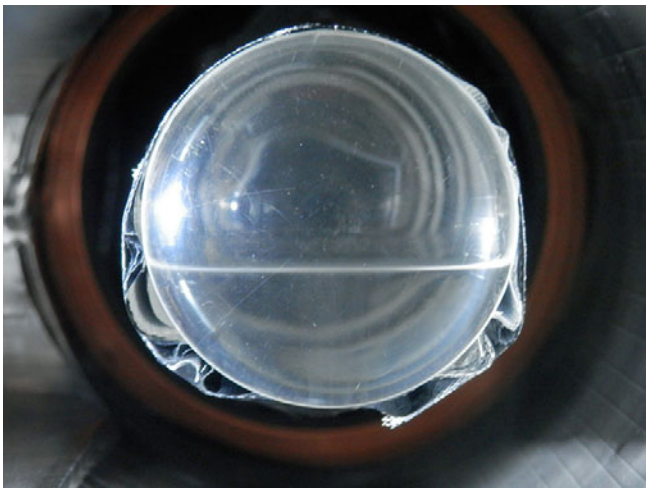

Fig. 8. (Color online) Front view of the target during the filling phase. The liquid-gas interface of hydrogen is clearly visible.

4.1 The cooling system

The hydrogen is liquefied in a cryostat equipped with a cryo-cooler (cold head on top of the cryostat and compressor in the vicinity of the cryostat) from the SUMITOMO company. A power of 10 W at 20 K is needed for the operation. The hydrogen is liquefied in the condenser (second stage of the cold head) and falls by gravity into the target through its circuitry. Inside the cryostat, a screen at 30 K is mounted on the first stage of the cold head. The screen protects all cold parts such as the condenser and the aluminum target support at 20 K from the 300 K radiations. A turbo molecular pump in combination with a hermetic primary pump is used to achieve a good vacuum in the cryostat. All pieces of equipment used in the setup are specially designed for an environment in contact with hydrogen.

4.2 The control-command system

The MINOS control system operates safely the target and detectors. It manages the vacuum and cryogenic system for the target and the gas system for detectors. The control system is composed of one Programmable Logic Controller (PLC) connected with remote I/O devices like pneumatic valves and low-temperature measurement device (CABTF, Centrale d'Acquisition Basse Température Fipée) through Profibus DP (Process Field Bus - Decentral peripherals). The PLC is connected to a Supervisory Control And Data Accquisition (SCADA) named Muscade^{TM}through a dedicated Ethernet protocol (see fig. 9).

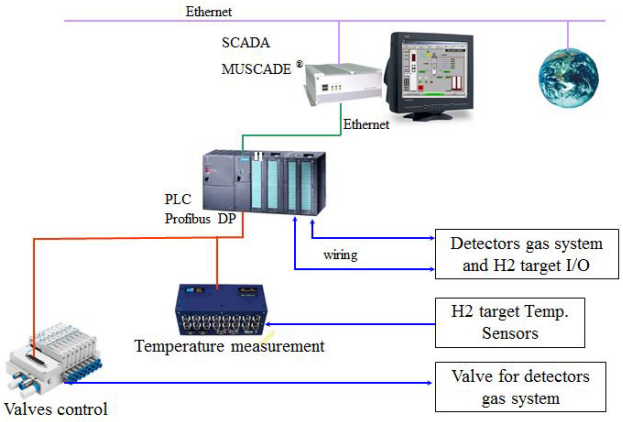

Fig. 9. (Color online) Control system architecture.

A temperature measurement device allows to connect all the resistive cryogenic temperature sensors and to deliver to the PLC the resistance value and the converted temperature. This device also manages the default sensor like short wiring or disconnections. It allows to connect 16 resistive sensors like Cernox and carbon temperature sensors, as well as displacement sensors.

The MUSCADE SCADA system developed at the Systems Engineering Division (SIS) of IRFU also manages the acquisition of all the data exchanged with the PLC. It offers tools to replay the acquired data directly on the same display and therefore to folllow in details all operations of the system. It also allows a remote connection through an internet client. In this configuration, a remote user is able to display the local system without possibilities to pilot it. In the MINOS case, it allows to bring a remote assistance to users during physics operation. For reliability purposes, the SCADA is integrated in a fanless PC and all the configuration is written on a flash memory card.

4.3 The target cell

The target cell is composed of two parts: the entrance window (110 μm thickness in polyethylene terephthalate (PET) film reffered in the text as the trademark Mylar and 40 mm in diameter, leading to an effective target diameter of 38 mm) and the exit window (150 μm thickness, 52 mm in diameter and 150 mm of length), both glued on a stainless target holder (see fig. 10 and 11).

The caps are thermoformed at 160 °C by mechanical stamping using dedicated tools to obtain the desired geometry. The considered glue withstands low temperatures ($T < 77$ K) and remains elastic to overcome the differential shrinkage of the materials used at 20 K (Mylar, aluminum and stainless steel). Therefore, it ensures the sealing between the different parts of the target. In addition, two aluminum rings are placed around the envelope of Mylar on the stainless steel part [27].

By contraction at low temperature, these rings strengthen the pasting against the internal pressure efforts, which could reach a maximum of 1500 mbar absolute pressure (abs).

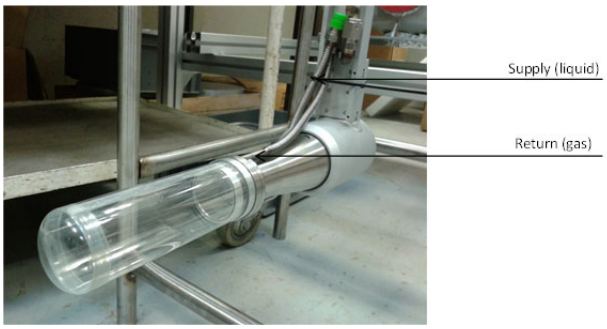

Fig. 10. (Color online) Front view of the target cell mounted on its aluminum support. Supply and exhaust tubes for hydrogen are visible.

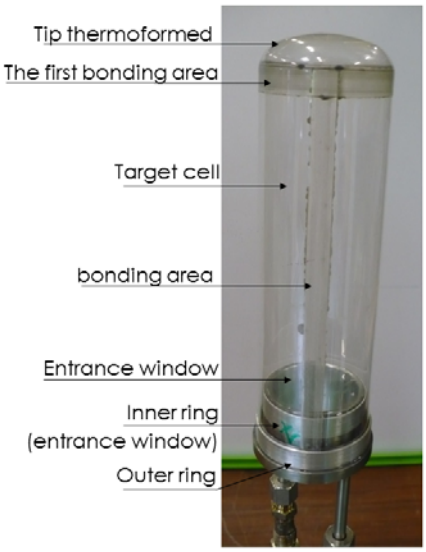

Fig. 11. (Color online) Side view of the target cell. The different sub-parts of the target are indicated with arrows. The target is cylindrical.

To estimate the necessary thickness of the Mylar windows we use the ASME code [29] (recommended by Fermilab and the Jefferson laboratory (US)) and the Timoshenko model [30]. After the Mylar windows sizing, the burst pressure was checked at both room temperature and liquid-nitrogen temperature. The safety rules of Fermilab (US) recommends a burst pressure for Mylar at least of 2.8 bar (internal differential pressure). Crash tests have been preformed with liquid hydrogen five times. The burst pressures reached values from 5.5 bar to 6.3 bar, well above the widespread Fermilab safety rules.

Note that the end caps of the target, both for the entrance and exit windows, are not flat but curved from both the production technique of the exit window and the pressure difference when the target is filled. The flexure at entrance window is estimated to be 2 mm. An error of 10% on this flexure value is estimated since it cannot be measured at 20 K. The exit window is rigid and its deviation from a flat end cap is 4 mm along the symmetry axis. A good precision of the effective target thickness profile is important since the energy loss reconstruction of the

projectile or residue is a key aspect for optimal use of the MINOS device. The foreseen silicon strip detectors at the entrance and exit of the MINOS device should ensure the reconstruction of the projectile and residue position onto the entrance and exit windows, respectively, at a 1 mm FWHM precision. The variation of thickness target thickness due to the curvature of the windows is small compared to this position resolution ($\delta z/\delta r < 0.2$, with δz thickness variation along the beam axis for a radial shift of δr). Hence, the effect will be negligible compared to the vertex position reconstruction resolution.

4.4 Safety considerations

This cryogenic system operates in a closed loop. The target is connected to a 800 liters storage tank via two check valves. The total quantity of hydrogen is 1200 liters (107 grams at normal temperature and pressure) for a 150 mm target. The initial load of 1500 mbar (at room temperature) in the storage tank is required to obtain a full liquid target. Hydrogen is liquefied in the condenser and supplies the target in a second loop inside the cryostat. The amount of liquefied hydrogen is 350 cm^3 (volume of the target) and the final pressure is 1025 mbar (abs) at 20.3 K in the circuitry and 1050 mbar in the storage. According to the Fermilab regulations, storage and use of flammable gases at physics experiments, this system is classified as risk class 0 (H_2 volume < 7400 l).

Apart from using procedures, tools and material consistent with hydrogen installations, safety is mainly guaranteed by the following requirements: i) minimizing the amount of hydrogen in the system, ii) operating pressure of 1050 mbar at 20 K (target filled), iii) using passive safety in the cryogenic rack (check valves with low $\delta P = 1$ PSI), iv) testing the pressure resistance of target cells via bursting tests for windows at both room and cryogenic temperatures, v) avoiding over-pressure accident. In case of rupture of the target cell, the hydrogen flows to the cryostat (100 liters), in the vacuum storage (280 liters) and storage tank which acts as a second container. The maximum pressure in the cryostat and the vacuum chamber is 770 mbar absolute and 1050 mbar absolute for the storage tank. The residual gas in the vacuum chamber is later evacuated by pumping.

5 Vertex tracker

5.1 General overview

As shown earlier, the MINOS tracker is a compact cylindrical gaseous detector composed of an annular Time Projection Chamber (TPC) surrounded by an external Micromegas tracker. The TPC is used to reconstruct the proton tracks in three dimensions and localize the vertex position of their origin in the liquid-hydrogen target. The TPC is read out on one side by a bulk-Micromegas detector [31,32] which is segmented in pads. The external cylindrical bulk-Micromegas layer is used for TPC electron drift velocity calibration and as a complementary trigger. It is segmented in C-shaped (semi circular) strips to localize the tracks crossing the TPC volume along the beam direction (*i.e.* the electron drift direction).

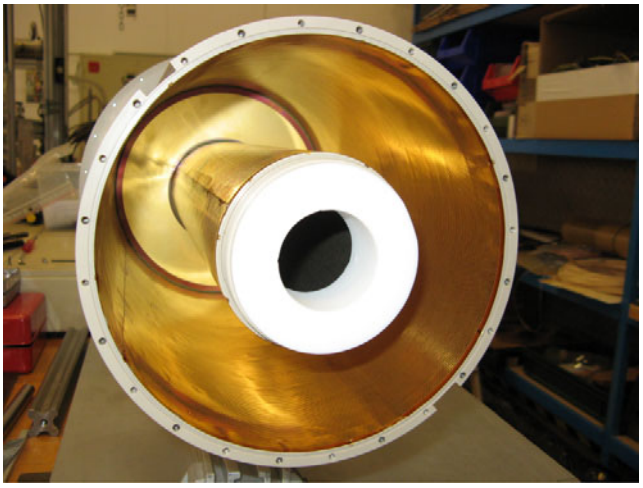

Fig. 12. (Color online) Picture of the MINOS TPC field cage.

Besides the need of compactness, the design of the TPC vessel requires a light structure to keep a low radiation length. The chosen design can be reached by use of a cathode high voltage as low as possible. This is the case with the current baseline TPC gas mixtures for which the electric field is fixed below 300 V/cm.

The 300 mm long TPC vessel (see fig. 12) is greatly inspired by the design of the PANDA TPC [33]. It is composed of an internal and an external concentric cylinders made of 2 mm thick Rohacell®(polymethacrylimide low density rigid structural foam) material, 80 mm and 178.8 mm internal diameters respectively. The outer surface of the internal cylinder and the inner surface of the external cylinder are each covered by a gas tight copper-stripped Kapton (polyimide) foil which define the internal and external electric field cages. The external vessel diameter is chosen for the TPC to fit with the DALI2 γ-detector acceptance. The two endcaps, the cathode plane and the Micromegas readout plane, are mounted on both sides of the vessel with 1 mm diameter O-rings in order to be able to easily replace them or to open the TPC vessel in case of a field cage electrical failure. The backside of the cathode endcap holds the gas outlets, the high-voltage connections for the cathode plane and the first strip of the field cages. The backside of the Micromegas endcap holds the gas inlets and the high-voltage connections for the Micromegas mesh and the last strip of the field cages. The cathode plane printed circuit board (PCB) is a sandwich of two 1.6 mm thick glass epoxy layers on both sides of a 50 μm thick Kapton foil used to increase the dielectric strength of the assembly and sustain up to 9 kV cathode voltage with a sufficient safety margin. It was manufactured by CERN/TE-MPE-EM division.

Because the MINOS TPC has a small volume of 6 liters and will be typically used in typical experiments of one week, it was chosen to feed the TPC with a nominal 10

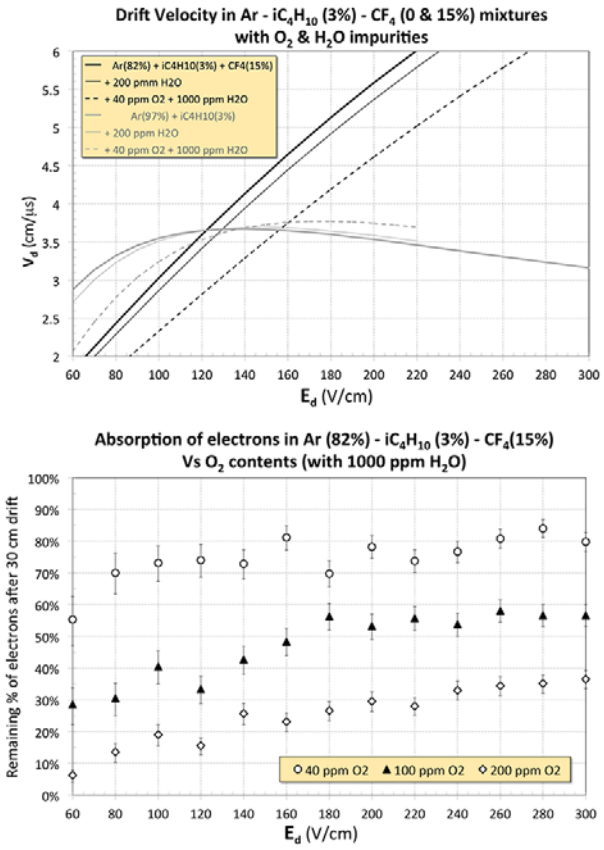

Fig. 13. (Color online) Magboltz simulations [23] of the gas characteristics. Top: Electron drift velocity as a function of the drift electric field for the two MINOS TPC gas candidates gas candidates (in black the Ar(82%)-iso(3%)-CF_4(15%) gas admixture, and in grey the Ar(97%)-iso(3%) admixture) and for different oxygen and water contents. Bottom: Electron attachment after 30 cm drift in the baseline MINOS TPC gas with respect to oxygen impurity content.

liters per hour gas flow by use of premix B20 bottles. The TPC gas pressure is fixed at 5 mbars above atmospheric pressure with a bubbler located on the TPC exhaust pipe. The drift velocity and absorption of drift electrons are significantly sensitive to O_2 and H_2O impurities in the volume of the TPC as illustrated in fig. 13. Two monitors are connected to the TPC output gas line to measure the level of water and oxygen content in the outpout gas. In the nominal conditions, a 40 ppm oxygen and a 900 ppm water contents were measured after 1 day of argon gas flushing with a first fully assembled TPC prototype. These levels of impurities are correlated to the gas tightness of the TPC vessel, the materials in contact with the gas (copper, Kapton, glass epoxy) and the gas flow.

5.2 Micromegas pad-plane detector

The Micromegas detector was invented by I. Giomataris, G. Charpak, Ph. Rebourgeard and J.-P. Robert in the Detector, Electronics and Computing division of CEA in 1995 [34]. The principle can be described as follows: the gas volume is separated by a thin micromesh in two regions, one where the ionization and drift of the electrons occurs and one, typically 100 μm thick, where the amplification takes place. In the amplification region, a high field (40 to 70 kV/cm) is created by applying a voltage of a few hundred volts between the mesh and the anode plane, which collects the charge of the avalanche. The anode is segmented into strips or pads. The advantages of Micromegas are due to the amplification gap and the configuration of the electric field on the two sides of the mesh, itself depending on the mesh pitch. The gap being very small, the size of the avalanche and hence the signal rise time are very small, leading to an electron signal of a few nanoseconds and an ion signal less than 50–100 ns, for most gas mixtures. Such ion collection allows high rates to be sustained. Another relevant property of Micromegas for use as a TPC charge amplification readout is the backflow of ions in the TPC drift space which is at a percent level with a standard detector geometry [35].

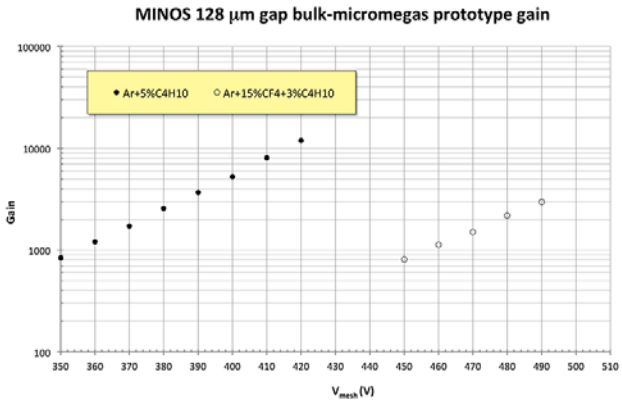

Fig. 14. (Color online) Measured amplification gain of the bulk Micromegas detectors as a function of the mesh potential. Gains are shown for two gas admixtures.

The MINOS TPC uses the standard so-called bulk Micromegas with a 128 μm amplification gap [32,36]. This Micromegas technology is well known for its robustness, simplicity and performances formerly illustrated in the TPCs of the "near" detector of the T2K experiment [37]. The choice of this technology for MINOS was particularly driven by the need of a very compact design as it shows very good uniformity of performances.

As quoted before, a gas mixture composed of argon (82%), CF_4 (15%) and isobutane (3%) has been retained as a baseline for the TPC. Its electron drift velocity (see fig. 13) can be tuned to match the optimum one with respect to the sampling frequency of the readout electronics (5.8 cm/μs for 100 MHz). It keeps electron transverse and longitudinal diffusions below 200 $\mu\text{m}/\sqrt{(\text{cm})}$ and the gain of a 128/μm bulk-micromegas can reach a few thousands (see fig. 14). Attachment of electrons by oxygen impurities is also rather well contained in this fast gas if its content stays below a few ten ppm (see fig. 13).

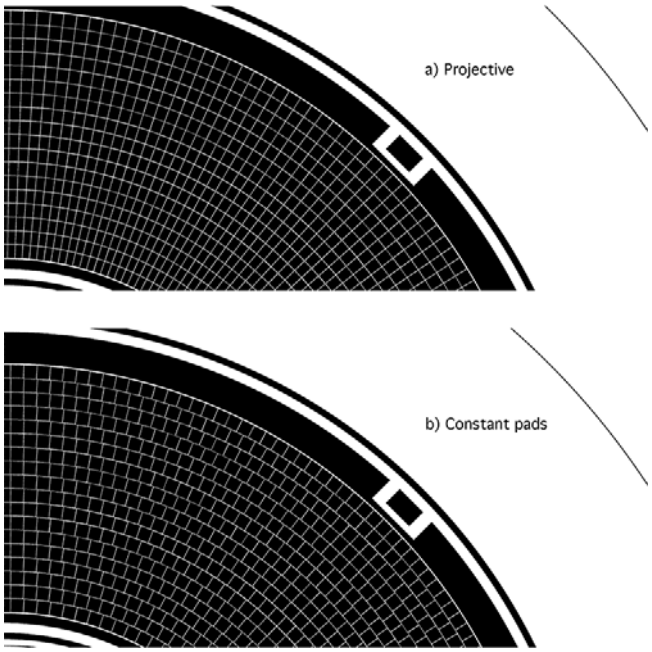

Fig. 15. Micromegas pad plane geometries: projective pad geometry (a) and constant pad geometry (b). The Micromegas mesh rectangular connection pad is also shown.

The same mixture without CF_4 has the advantages to saturate the electron drift velocity at 140 V/cm drift electric field and to reach higher Micromegas gains with lower spark probability. Its drawbacks are 3 times larger transverse and longitudinal diffusions and a lower electron drift velocity. The definitive choice of the MINOS TPC gas mixture will be done after the results of the complete MINOS Vertex tracker in-beam characterization performed in october 2013 at HIMAC accelerator facility (Japan).

Two geometries have been considered to be used for the MINOS Micromegas detector (fig. 15): i) a projective geometry with cylindrical axis, the inner pads being smaller. From simulations, this feature is expected to improve the resolution on the vertex position but, on the other hand, less charge will be collected on these pads and the signal-over-noise ratio may not be sufficient for energetic protons. It corresponds to a radial azimuthal (r, ϕ) geometry which distributes the readout over 4608 pads arranged in 18 cylindrical strips of 256 sections each. In total 12 layers and more than 18000 vias are needed to route the signals out with a 3.2mm thick PCB. ii) A constant-area pad geometry (2 mm × 2 mm) which distributes 3604 identical pads. It provides a highly homogeneous readout including in the central area where the reconstruction accuracy is the most difficult to achieve. Both geometries have been designed. The printed circuit boards were manufactured by the ELTOS company (Arezzo, Italy) and the bulk-Micromegas mesh integration was done at the CEA/IRFU MPGD workshop. Designs of the bulk-Micromegas projective and constant pad planes are shown in fig. 15.

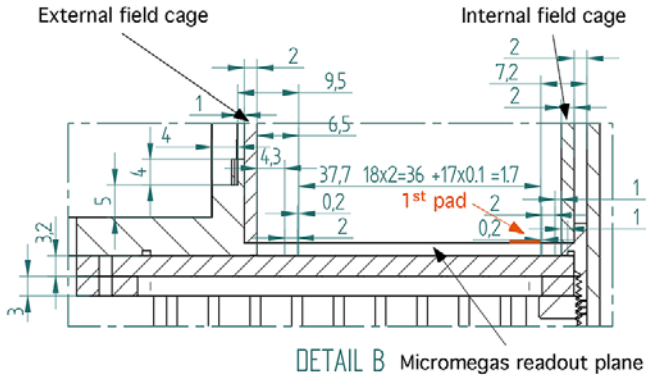

Fig. 16. (Color online) Detail drawing of the TPC endcap and of the connections to the field cage. Distances are given in millimeters.

5.3 Field cage

The MINOS-TPC electric field cage is a key component of the TPC since it defines the path the electrons released along the proton tracks will follow towards the Micromegas readout plane. The precision of the proton track 3D reconstruction and hence the precision of the vertex localization strongly depend on the uniformity, stability, and knowledge of the electric field lines in the TPC volume. For that purpose the bulk-Micromegas technology is well suited to maximize the uniform amplification area of the readout plane with only 3.2 mm between the TPC walls and the first active readout pad. The first active pad for track reconstruction is thus radially located as close as 7.2 mm from the exit of reaction chamber (see fig. 16).

The TPC field cage was therefore designed with the goal to radially reach a uniform electric field ($E_z/E_x \leq 10^{-4}$) at the first pad location. According to electric field simulations, this should be insured with an electric field cage made of 1 mm large strips printed with a 1.5 mm pitch on both sides of a 50 μm thick Kapton foil for an equivalent 0.75 mm pitch between top and bottom strips (see fig. 17). The first and last strip of the cages are, respectively, located at 4.5 mm below the cathode plane and 1.5 mm above the Micromegas mesh. Two 3.9 MΩ surface mount resistors (0805 size) are soldered in parallel between a top and its adjacent bottom strip for a total of 196 + 195 strips and 788 resistors. The field cage Kapton foils were manufactured at CERN/TE-MPE-EM workshop and the resistors were soldered at the cabling division of CERN/TE-MPE-EM. Eight 1 mm long strips on both sides of the Kapton foils are used to make the solder free connections between the field cages and the TPC endcaps. The impedances between two adjacent top strips are individually measured before the Kapton foil is glued on the TPC Rohacell®cylinder. Mean value of the measured impedance for the resistors is 3889.8 kΩ for a peak to peak dispersion of 0.25% (4 times better than the 1% manufacturer specification). At each step of the TPC vessels assembly, the TPC field cages are electrically controlled under 2000 V for a 2.63 μA expected output current. The 2 field cages are supplied in parallel through the cath-

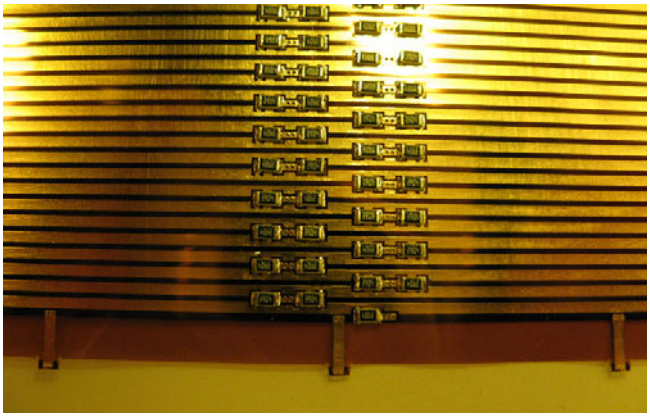

Fig. 17. (Color online) Zoom on the SMR resistors of the field cage Kapton foils.

ode high voltage and a separate high voltage is applied on the last strip to precisely fix it in accordance to the high voltage applied on the Micromegas mesh. A CAEN SY5527 multi-channel crate is used with one 12 channels 3 kV A1821H module for the high-voltage supply of the Micromegas mesh (TPC and external tracker) and the last strip of the field cages, and with one 6 channels 15 kV A1526 module for the high-voltage supply of the cathode. The current drawn in each field cage for the baseline gas mixture at 220 V/cm drift electric field is 8.2 μA, leading to 16.1 V between two adjacent field cage strips.

A field cage assembly first consists in the cylindrical modeling of the Rohacell®sheet with a precise positioning and gluing at 50 °C of the Kapton using a dedicated mandrel. The vessel cylinder is then removed from the mandrel and the 2 endcap rings are positioned and glued on the Rohacell®cylinder with a tool which is used to guarantee the cylinder length and the parallelism of the 2 rings at $\pm$0.1 mm on which the 2 endcaps planes will be later mounted with O-rings. The gas tightness of the field cage cylinders is checked to be less than 0.05 l/h. The final assembly of the two TPC vessels with the cathode and Micromegas readout planes is done in clean room. High-voltage tests are performed to control the electrical connections and the operation of the TPC at its nominal voltages with the TPC mounted around the electrically grounded reaction chamber tube. The TPC is fully shielded through the grounding of the external Micromegas cylinder layer, the internal grounding layer inside the Micromegas readout plane PCB and the grounded bottom side of the cathode plane PCB.

5.4 External Micromegas layer

The purpose of the external Micromegas layer is to obtain the information on the z-coordinate of the track independently of the TPC drift velocity. This will allow to measure any change of the electron drift velocity that may occur during experiments due to inexpected change of experimental conditions (gas impurities, temperature, ...).

Fig. 18. (Color online) Full external Micromegas layer mounted on the TPC. The outer side of the cathode (copper layer) is visible.

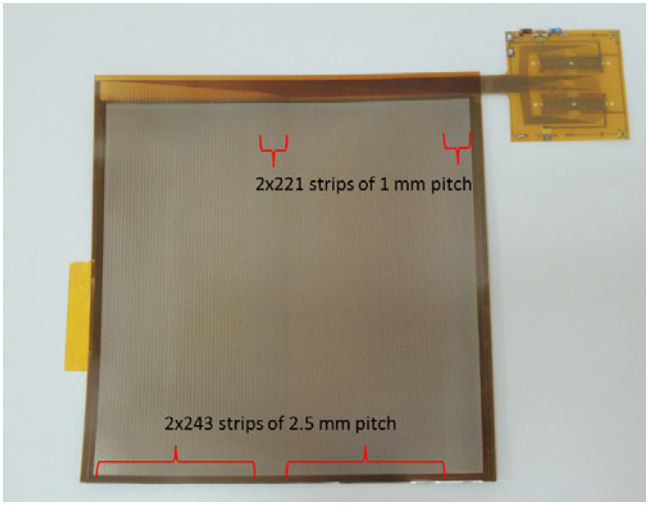

Fig. 19. (Color online) Picture of the external layer detection plan. Two strip widths are visible.

Furthermore, it can be used as an external trigger for the MINOS device.

The external layer detector has been built at the CERN/TE-MPE-EM and assembled at CEA Saclay. The particularity of the detector is to present a cylindrical shape made of curved Micromegas detectors with a radius of 92 mm (see fig. 18). Curved Micromegas have been developed at CEA Saclay for the CLAS12 project [38] and details are published elsewhere [39]. The anode (inner side) is 200 μm thick to ease the detector curvature radius and to reduce the radiation length and its capacitance. The external-layer detector is composed of two tiles

of 128 strips of 260 mm long. The number of strips has been chosen to limit the number of channels. Two different strip sizes cover the detector along the radial direction: the z-position of protons exiting the TPC can be measured thanks to 2×21 strips of 1 mm pitch. Other strips are wider: 2×43 strips of 2.5 mm pitch (see fig. 19).

The cathode (outer part) is a 200 μm thick of polyamide film covered by 5 μm of copper on both sides. A high voltage is applied inside the detector whereas the outer side of the cathode is connected to the electrical ground acting as a Faraday cage that prevents the MINOS vertex tracker against electromagnetic noise sources.

The drift gap between the cathode and the Micromegas mesh is 4 mm. Signals of the detector are read with the same electronics as the TPC.

6 Electronics

6.1 Requirements and constraints

MINOS is a medium-size experiment totalizing 5376 channels: 4608 channels for the TPC in the projective geometry, 256 channels for the cylindrical trigger detector, and 512 channels for the upstream and downstream beam monitor double-sided silicon strip detectors (DSSSD). This number of channels is too high for a cost-effective realization of the readout electronics with off-the-shelf commercial hardware. Performance requirements were found compatible with the characteristics of the AGET chip [40] developed by the GET [2] Collaboration. This device is a pin-compatible evolution of the AFTER chip designed for the T2K experiment [41]. It comprises 64 channels of charge sensitive pre-amplifier and shaper (120 fC to 10 pC range and 16 selectable values of shaping time) followed by a 512-time bin switched capacitor array writeable at up to 100 MHz and readable at 25 MHz with an external ADC. Assuming a typical occupancy of $\sim$ 8 channels hit per chip, the event data acquisition rate can reach a few kHz which is adequate to our needs. Magnetic field tolerance and radiation hardness are not required for the readout electronics of MINOS, but the relative small size of the TPC, the low material budget allowed in the region close to the pad plane and the desired compact geometry of the photon spectrometers inside which the MINOS apparatus should be immersed do not allow the readout electronics to be directly attached to detectors. We therefore had to place it outside of the detector volume and use cables for connections. This greatly relaxes space and power dissipation constraints for the electronics at the expense of thousands of additional cables and increased noise.

[2] GET (acronym for "General Electronics for TPCs") is a joint project between CEA-IRFU, CENBG, GANIL (France) and NSCL (US) laboratories. The project has been funded by the French funding agency ANR and the DOE (US). The spokesperson is E.C. Pollacco from CEA Saclay.

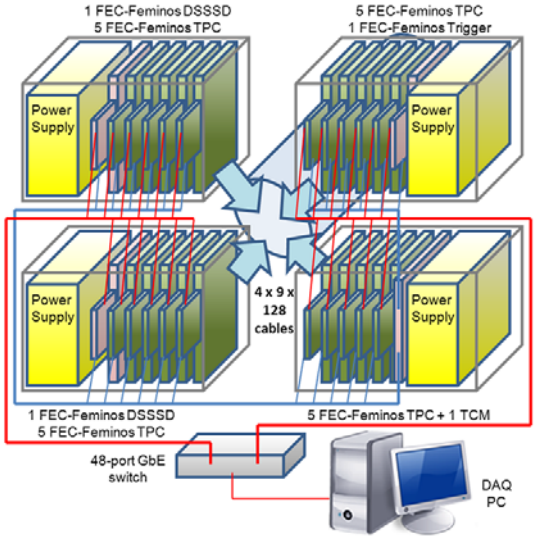

Fig. 20. (Color online) Architecture of the MINOS readout electronics.

6.2 Architecture concept

In order to provide a readout system, we devised an upgradeable system: the current setup re-uses the front-end cards (FECs) equipped with the AFTER chips that were produced for the T2K experiment. These cards will be replaced almost transparently from the hardware and software point-of-view by new FECs populated with AGET chips as soon as production is completed. The digital part of the T2K readout system is now obsolete and is inadequate in terms of data rate and throughput for MINOS. An entirely new board was designed to readout AFTER or AGET based FECs. This new board is called *Feminos*. Up to 24 Feminos can be synchronized to a common clock and trigger by a single companion card called the Trigger Clock Module (TCM). System configuration, monitoring and data aggregation from multiple Feminos to a common DAQ PC uses a commercially available Gigabit Ethernet switch and relies on the standard UDP/IP networking protocol.

6.3 System implementation overview

A schematic view of the readout system of MINOS is shown in fig. 20. It is composed of four crates mounted on the MINOS frame at about 60 cm upstream the TPC pad plane (see fig. 7). Each crate is populated with five or six 256-channel FECs, its associated Feminos and a 5V-20A PC-ATX low-voltage power supply. One of the crates contains the TCM. Five FEC-Feminos in each crate are assigned to the TPC (5120 channels are available although only 4608 at most are effectively used), one FEC-Feminos (256 channels) maps to the cylindrical external-layer detector, and the last 2 FEC-Feminos (512-channels) are connected to the beam monitor DSSSDs. The 23 Feminos are connected to the TCM via 2 m CAT 6 RJ45 patch

cords and are connected with a second cable to the DAQ through a 48-port gigabit Ethernet switch.

6.4 Main system components

6.4.1 Detector readout cables

The TPC pad plane is connected to the readout electronics by a set of almost five thousand 80 cm long cables. To reach the desired compactness and to maximize the signal-to-noise ratio, we followed the experience gained by internal R&D for the CLAS12 project [42] in using specially designed ribbons of micro-coaxial cables made by Hitachi Cable Ltd. The FC-Band(R) KZ12-305 product is a flexible (less than 2.5 cm bending radius), 24 mm wide and 0.4 mm thick ribbon composed of sixty-four 44 AWG micro-coaxial cables. Each micro-coaxial cable is only 0.35 mm in diameter and has a very low capacitance of 50 pF/m. Two KZ12-305 ribbons are soldered side-by-side on an adaptation PCB at each end to make a 128-channel cable assembly. The TPC end of the cable is equipped with a 140-pin 0.8 mm pitch connector (ERM8 series from Samtec) while the extremity that connects to the electronics has two 80-pin 1.27 mm pitch connectors from ERNI. In total, thirty-six 128-channel cables are needed to readout the TPC. Six additional cables are needed to readout the trigger detector and the DSSSDs. These cables are similar to those used by the TPC except for the length which is ~ 1.4 m and the detector end PCB which has two 80-pin 1 mm pitch FSI connectors from Samtec.

6.4.2 Front-End Cards and Feminos

The FEC contains four AFTER or AGET chips, the passive protection circuit for the 288 input channels (256-channel in the AGET version), a quad-channel ADC (Analog Devices AD9229), an on-board pulse generator for test and calibration, and some glue logic. One of the differences between the AFTER and AGET chips is that all channels have to be digitized in AFTER while AGET has a discriminator on each channel that allows only hit channels to be read-out. This reduces dead-time accordingly. Each FEC is controlled by a Feminos which contains all the necessary logic to readout data, perform elementary processing such as pedestal subtraction and zero-suppression, and encapsulate data in Ethernet Jumbo frames for transmission to the DAQ PC. The Feminos houses a commercial FPGA module, the Mars MX2 from Enclustra Gmbh [43]. This low-cost, standard SO-DIMM form factor module, features a Xilinx Spartan 6 FPGA, 128 Mbytes of DDR2-800 SDRAM, 16 Mbytes of compact flash, a Gigabit Ethernet PHY and ~ 90 user I/Os. Optimized FPGA firmware and software for the embedded MicroBlaze softcore processor was developed on the Feminos to exploit the full performance potential of the AFTER and AGET chips. More details on the design and performance of the Feminos are presented in [44]. A photograph of a FEC connected to its Feminos and two detector cables is shown in fig. 21.

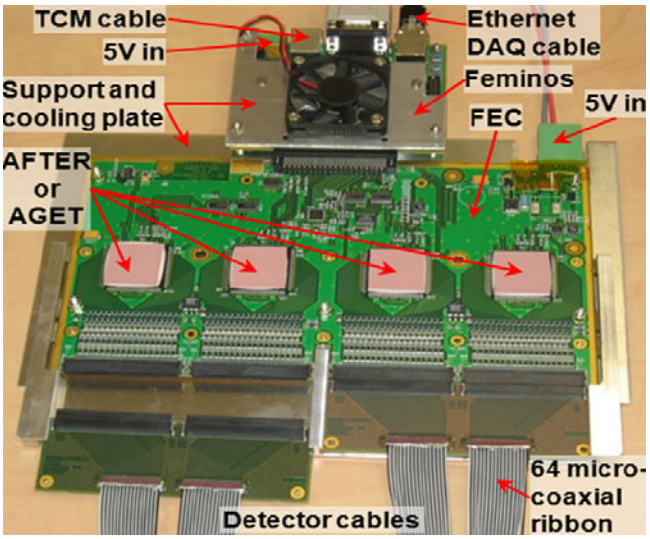

Fig. 21. (Color online) A FEC with its Feminos and detector cables.

6.4.3 Trigger Clock Module (TCM)

The main roles of the TCM are to distribute a common 100 MHz reference clock and trigger signals to all Feminos and to merge dead-time information from all Feminos into a single trigger hold-off signal. The TCM can provide the master reference clock or it can receive it from an external source in NIM or LVDS format. The TCM has several I/Os in LVDS, NIM and LVTTL standards, to receive an external trigger signal, a synchronous timestamp clear input, an event count clear input and a busy output. The fan-out to the Feminos is made in LVDS over standard RJ45 cables (cat. 6 TP). The core component of the TCM is also a Mars MX2 FPGA module and the TCM shares a large fraction of the software for the embedded MicroBlaze processor with the Feminos. The TCM is connected to the DAQ PC via a Gigabit Ethernet link but this is only used for configuration and system performance monitoring (transfer of dead-time histograms, measurements of event throughput, error counters, etc.).

6.5 Performance summary

One of the important figures of performance is the noise level of the detector and front-end pre-amplifier chain. Without cable and detector, measurements on a FEC show that the typical noise is $\sim$ 850 electrons r.m.s. (120 fC range, 200 ns shaping time and 100 MHz sampling clock). Figure 22 shows the pedestal noise measured with an AFTER FEC connected to the TPC via 80 cm long micro-coaxial cables under the above settings of the elctronics. The average noise is $\sim$ 1500 electrons r.m.s. which meets our requirements.

Important parameters for the data acquisition are the sustainable event rate and data throughput. When the DAQ is not the limiting element (*i.e.* the amount of event data to be collected is sufficiently small compared to the

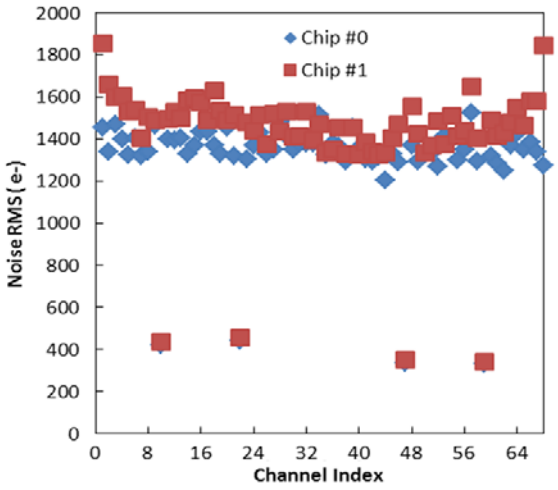

Fig. 22. (Color online) Pedestal noise measured on 128 TPC channels. The points with lower noise correspond to 4 extra channels of the AFTER chip not connected to package pins.

available link bandwidth), the sustainable event rate by a Feminos and FEC is measured to be $\sim$ 590 Hz with AFTER chips (511 time-bins readout per channel) and is $\sim$ 5.5 kHz with an AGET FEC for 6 channels hit per chip and 512 time-bins readout per channel. These figures correspond to more than 90% of the theoretical limit that can be reached with the AFTER and AGET chips. When event size is the dominant limitation, the achievable event rate is determined by the available DAQ bandwidth which is measured to be $\sim$ 110 Mbyte/s for one Feminos and $\sim$ 123 Mbyte/s (*i.e.* Gigabit Ethernet link saturation on the DAQ PC side) with multiple Feminos. The actual data taking rate in experimental conditions may approach the limit of 590 Hz when using AFTER chips, but reaching higher event rates with AGET critically depends on low hit count in the TPC, *i.e.* the per-channel discriminator of the AGET chips have to be set to achieve a good separation between the few expected real tracks and background hits caused by noise. These tuning and measurements remain to be done. Power consumption for a FEC (AFTER or AGET) and its Feminos is 2 A at 5 V which translates into less than 40 mW/channel. Active air cooling is sufficient for this system. A small fan is placed on the cooling plate of each Feminos and each crate has three large fans. In operation, the temperature reported by the sensor of each Feminos remains below 45 °C at a room temperature of $\sim$ 25 °C.

In increasingly resource-constrained projects, low manpower effort, fast development cycle and cost effectiveness are also important figures of merit. With significant hardware re-use, a strategy of compatibility between successive front-end ASIC generations, a simple and scalable architecture, the choice of a ready-to-use FPGA module and the adoption of a generic software framework, the development of the whole readout hardware and software for MINOS required $\sim$ 2 FTEs during $\sim$ 2 years. The production cost of the electronics, cables and cooling plates corresponds to $\sim$ 8 euros/channel which is justified by the advanced technology used. Minimal complexity flat aluminum plates for the mechanical support, shielding and cooling of the electronic cards have been designed. Power distribution uses very low cost PC-type power supplies and cables assembled internally. Computing and networking relies on commercial commodity products.

7 Data acquisition software

The MINOS DAQ software that runs on a DAQ PC is based on a new C++ generic DAQ framework named Mordicus. This framework is developed in parallel with the MINOS-specific parts of the software. Mordicus is a generic implementation of the concepts previously used to develop the DAQ software of the KM3NeT [45] and GET projects. It supports standalone operation and provides the interface to a master level of DAQ, run control and data storage when MINOS is used in conjunction with DALI2 or other detectors.

7.1 Requirements

The MINOS readout electronic is composed of 23 Feminos-FEC and one TCM board for clock, trigger and deadtime synchronization. They are connected to a single DAQ PC (equipped with two network interfaces) through a 48-port gigabit Ethernet switch, which is enough to handle the expected data rates ($\sim$ 160 Mbit/s). Both Feminos and TCM boards run a UDP/IP-based command server for configuration, monitoring and dataflow control. Data are sent to the client in standard size Ethernet frames or Jumbo frames up to 8 KB. The role of the DAQ software is to configure and monitor Feminos and TCM boards, and collect and store raw data corresponding to detector-wide events.

7.2 Architecture

The main concepts behind Mordicus are:

1) An object-oriented framework factorizing DAQ concepts and defining C++ interfaces allowing user-defined implementations to be provided through factories and plugins.
2) A distributed and scalable system based on specialized worker processes, which can run on a single PC or on computer farms. There are three main worker process categories:
   i) Data Generators: responsible for data readout from the electronic subsystems.
   ii) Data Processors: responsible for event building, filtering and storage. They can be further specialized when scaling-up the system, in order to process data on PC farms.
   iii) Data Controllers: responsible for interfacing with boards that do not produce data.

3) A centralized client-server model for Run Control: a single Run Control Server controls all worker processes and accepts connections from one or many clients which can be GUI-based or not.
4) A robust slow control system, based on a state-machine distributed across the workers and synchronized by the Run Control Server.

Mordicus is partially based on the ZeroC Internet Communication Engine (ICE) middleware [46]: a framework allowing distributed application to communicate through network using high-level object-oriented abstractions and simplifying their management. Mordicus particularly uses the IceGrid Registry which acts as a name server to reference remote objects and servers by name instead of IP addresses and ports, thus greatly simplifying configuration and deployment.

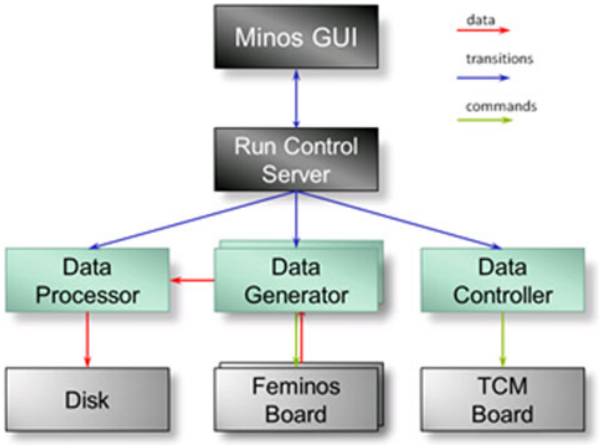

Fig. 23. (Color online) Architecture of standalone MINOS DAQ software.

7.3 Implementation

Figure 23 shows the processes composing the MINOS DAQ software and how they communicate and interface with the hardware. Currently, there is one Data Generator process per Feminos board, therefore there will be a total of 23 Data Generator processes on the final system.

Each Data Generator is responsible for the configuration and data acquisition of its associated board. It receives UDP frames containing event fragments, handles potential fragment loss, and sends a reliable TCP stream of well-formed events to the Data Processor. The Data Processor receives the event streams from all Data Generators. When event reconstruction is enabled, it merges the events having the same event number and timestamp and coming from different sources in order to create complete events containing the data of every enabled Feminos. Finally, it can store these assembled events to disk. The Data Controller does not perform any data acquisition or processing, but it is required to configure the TCM board.

The Run Control Server is responsible for the orchestration of Run operations; it acts as a front-end between the many processes composing the acquisition system and the outside world. It can control any number of nodes: their list is specified by the run control configuration. The Run Control Server runs a state-machine and ensures synchronization between its state-machine and the state-machines of each worker process. Figure 23 exposes the state-machine of the Run Control. When a Run Control client (eg: MINOS GUI) takes the lead of the Run Control Server it sends a connect event, passing the run control configuration as parameter. It triggers the connection of the server to each Data Processor/Generator/Controller listed in the configuration and enabled. Then, the client sends the daq configuration to the server and sends the configure event. It will in turn trigger the configuration of all workers, by broadcasting them the configure event with the configuration as parameter. State-machine event broadcasting order is configurable (*e.g.* first the Data Processor, then the Data Controller, and finally all Data Generators concurrently).

The MINOS configuration is expressed using the "CompoundConfig" library [47] originally developed for KM3NeT. This is a generic configuration library allowing the description of hierarchical configurations with a powerful inheritance mechanism allowing definition of default values for series of similar objects while being able to locally override them. The library also benefits from a user interfaces and a database mapping which will be used to store configuration alongside with run metadata.

7.4 Coupling to an external DAQ

The Mordicus framework and MINOS DAQ have been designed from the beginning to be flexible enough to be integrated with an external DAQ system, such as Riken RIBF-DAQ [48] since the detector is expected to be used in conjunction with DALI2 and other detectors.

In the case of coupling to an external DAQ, the external DAQ takes over the Run Control Server. It requires a small state-machine client module to be integrated into the external software, so that start and stop commands are forwarded to the MINOS Run Control Server.

Even if the configure order is issued externally, the selection of our system configuration is under our responsibility. Consequently, our system separates state-machine control from configuration selection: the MINOS GUI keeps control over configuration, but leaves state-machine operations to the external DAQ. It means that configuration selection occurs on the Run Control Server but has no immediate effect: it will only be applied the next time a configure event is sent to the Run Control state-machine. It is possible to deal with systems that only have a start/stop step but no configure step: the configure can be automatically executed on start as needed (if the configuration has changed).

As an example of such coupling, Figure 24 shows how our DAQ integrates with the Riken DAQ: what makes the interface between both systems is a modified Riken babies process [48]. We had to insert run control client code so that start and stop commands are forwarded from

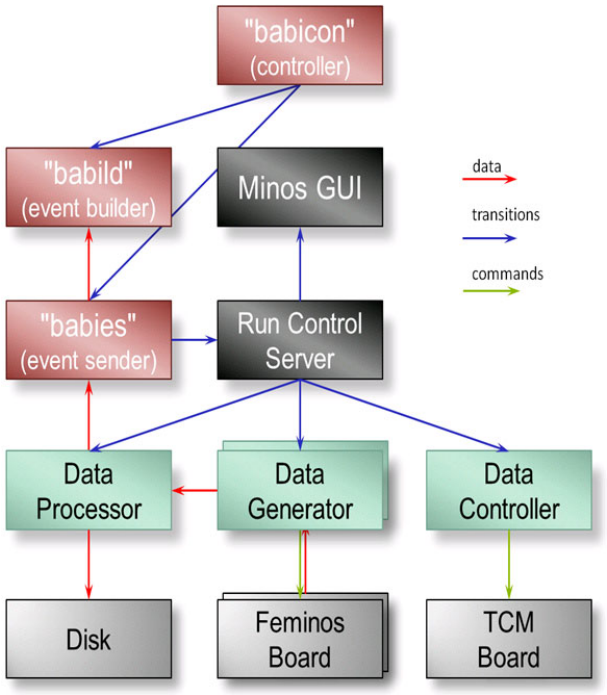

Fig. 24. (Color online) Architecture of the coupling of the MINOS DAQ software with the RIBF DAQ.

the babicon command-line controller to our Run Control Server. We also had to integrate a TCP server thread that transcodes data sent from the Data Processor by a standard TCP sender into the RIDF format, and forwards it to the babild event builder.

A complete integration between detectors requires merging MINOS events with the others detectors events, so data must be sent to the external DAQ. Beyond simple disk storage, the Mordicus framework was designed to allow any number of consecutive and user-defined data processing steps to take place after event building. It is then possible to implement a data sender that will transcode the data to the target DAQ format and send it through TCP, Unix sockets, pipes, etc. while keeping the local disk storage step. Extra features of the MINOS DAQ, such as more developed communication with the master DAQ, may be implemented for future applications if required.

8 Cosmic-ray validation

The full TPC system has ben validated at CEA Saclay on a cosmic-ray bench. In physics experiments, the MINOS TPC will track protons with a maximum energy of 300 MeV, leading to an energy loss of about few keV per mm. Cosmic rays are a relevant first validation as they lose about 1 keV/mm. The CLAS12 cosmic-ray test bench [39] at CEA has been used to test for the first time our vertex tracker. In the following, we illustrate results from these first measurements. A full qualification of the TPC capacities, from cosmic-ray measurements and upcoming in-beam measurements, will be published later.

Fig. 25. (Color online) Artist view of the CLAS12 cosmic bench composed of two plastic scintillators for trigger, large position-sensitive Micromegas detectors interspersing the MINOS TPC. Cables and electronics are not drawn for clarity purposes.

The experimental setup is illustrated in fig. 25. The cosmic bench is composed of i) two XY detection planes placed at the top and the bottom of the vertex tracker and ii) two plastic scintillators that are placed on the top and on the bottom of the whole structure. Each of these XY detection plane is composed of two $500 \times 500\,\mathrm{mm}^2$ Micromegas detector planes, with their strips orthognal between each other. These detectors are designed to reach a spatial resolution inferior to $300\,\mu$m. They are used to give two reference points along the cosmic ray track. The time signals of the scintillators are transmitted to a coincidence module in order to constitute the trigger of our data acquisition when a cosmic ray passes through the whole bench.

The TPC with the projective Micromegas plane geometry was inserted in this bench. The signals from the TPC and from the XY detection planes were all read with the MINOS electronics composed of FEC cards equipped with AFTER chips and Feminos cards for each quarter of the detection plane (see sect. 6).

Data taking was performed with the following settings for the electronics: 100 MHz sampling frequency, 120 fC range and 420 ns shaping time. The gas used was a mixture of Ar (82%), isoC_4H_{10}(3%) and CF_4 (15%). The cathode was set to 6 kV voltage and the Micromegas stage was set to an amplification gain close to one thousand. During the data taking, O_2 impurities were maintained below 60 ppm and H_2O impurities below 1000 ppm.

In a first step, raw data were extracted from the acquisition files and stored in a ROOT tree, containing simply the charge deposited in every pad of our Micromegas projective plane in our acquisition window of $5.1\,\mu$s. A fit of each pad energy signal collected over time was performed with the analytical function of eq. (7). The baseline $E_{baseline}$ was fixed in the electronics to 250 bins and

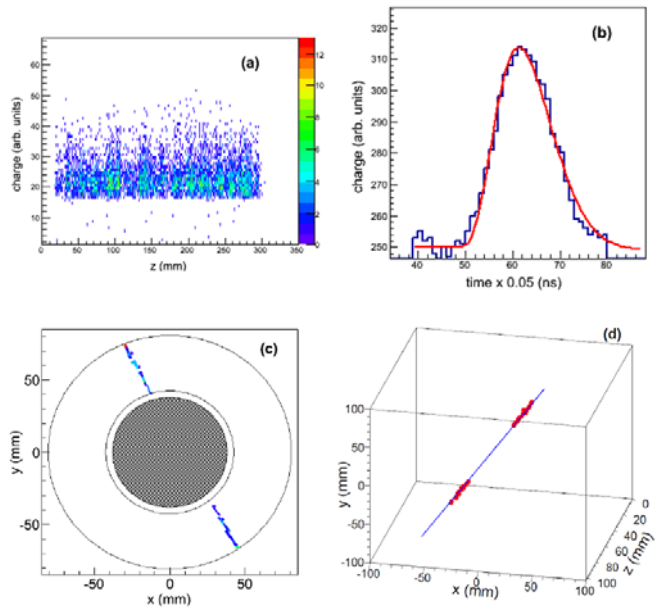

Fig. 26. (Color online) (a) The distribution of deposited charge as a fuction of the z-axis of the TPC for about 2000 events. (b) A typical signal collected on a pad. (c) Projection of a Track on the Micromegas plane. Background events above threshold have been left on purpose and can be seen at random positions on the pad plane. (d) 3D view of the event shown in 2D in panel (c).

substracted from the data, which leaves two parameters to be determined by the fit: the maximum and the timing of the channel relative to the trigger received by the electronics. The fit methodology is similar to the simulations described in sect. 2.1. An example of the quality of the fit can be seen on the event shown in fig. 26.

We have verified that the drift velocity corresponds to the one obtained via Magboltz simulations. Figure 26(a) shows the distribution of deposited charge as a function of the z-axis of the TPC. The distributions ends at 30 cm, corresponding to the lenght of the TPC. This shows that: i) the expected drift velocity of 4.74 cm/μs allows to obtain the correct value of z; ii) the charge collection is efficient all along the TPC axis. A typical signal collected by one pad is shown in fig. 26(b) together with its fit from eq. (7). The projection of the track of one cosmic ray on the Micromegas plane is shown in fig. 26(c), while the 3D reconstruction of the track is plotted in fig. 26(d).

9 Conclusion and perspectives

MINOS, a new device for prompt spectroscopy from fast nucleon knockout from hydrogen has been developed. The technical developments were presented in this article. Most important developments to be highligthed are i) a thick liquid-hydrogen target from a unique technique developed at CEA Saclay resulting in a thin-window long cell (up to 200 mm) filled with hydrogen, ii) a compact cylindrical TPC based on a 5000-channel Micromegas amplification plane with minimal radiation length built to surround the pipe in which the hydrogen target is inserted, iii) a modular readout electronics based on the T2K and GET developments allowing a digital sampling of all channels at 100 MHz over 12 bits. The TPC coupled to its full electronics has been recently further characterized through an in-beam measurement. Results on the intrinsic resolution of the system and details on the track analysis will be detailed in a forthcoming publication.

At this stage, MINOS is ready for operation at radioactive ion beam facilities with beam intensities greater than 150 MeV/nucleon. Very soon the electronics will be upgraded by replacing the AFTER chips with AGET chips, allowing a much larger data acquisition rate with individual-channel discriminators. From simulated multiplicities of TPC channels during $(p, 2p)$ experiments, the maximum rate that MINOS can handle is expected to be of the order of a few kHz, well above the expected trigger rate of the intended low beam intensity experiments.

MINOS offers access to the first spectroscopy of a new range of very exotic nuclei, beyond current reach. Compared to existing setups, its use will increase today the experimental sensitivity by a factor from 5 to 50, depending on the measured observable. It is aimed at being used at the RIBF of RIKEN from 2014 for both prompt γ spectroscopy and invariant mass measurements. In a later stage, it should provide unique opportunities at new generation fragmentation facilities such as the FAIR facility. Indeed, in the case of prompt in-beam γ spectroscopy, its use in combination with new generation high-resolution Ge arrays, such as the AGATA array, should lead to an increase in sensitivity of 100 to 200 compared to current setups. The use of thick H_2 targets coupled to a MINOS-geometry cylindrical TPC inside a solenoid indicates strong potentialities for missing-mass measurements from low statistics $(p, 2p)$ reactions at intermediate energies which should be further investigated in the near future. The higher energies available in the future at FAIR should allow the use of target thicknesses close to the maximum production rate of secondary species with almost no limitation from the beam energy loss in the target. When incident energies will be high enough for strangeness production from hydrogen-induced reactions, a MINOS-type setup may be considered as a way to greatly increase the production of neutron-rich hypernuclei and sensitivity to their study.

This work has been funded by the European Research Council through the ERC Starting Grant MINOS-258567. This work has largely benefited from the cross-field expertise in the Nuclear Physics Division of IRFU: the authors are thankful to the CLAS12 hadronic physics group members and their inspiring work on Micromegas detectors in collaboration with the Electronics and Detector Division (SEDI) of IRFU. They also thank Marc Anfreville, Dominique Durand and their team from SEDI for useful discussions and the mesh integration of the bulk Micromegas detectors. The authors are deeply thankful to B. Voss from GSI who openly shared his experience on the development of the prototype of the PANDA TPC. Rui de Oliveira from CERN/TS-DEM workshop is deeply aknowledged for his advices and helpful discussions, as well as the

CERN cabling division for the cabling of more than 3000 SDM resistors on the field cage Kapton foils. The authors would also like to thank warmly E. Delagnes, Ph. Chesny, P. Colas, S. Aune and I. Giomataris from CEA-IRFU for their constant support and expert advises on this project. They are grateful to K. Kusaka, M. Nishimura, M. Sasano, Y. Yanagisawa from RIKEN and Y. Kubota from CNS for their support during the validation of the MINOS H_2 target at RIKEN. Thanks to A. Boudard and M. Combet for providing the O_2 and H_2O monitoring system. The authors are indebt to T. Motobayashi and H. Sakurai for their support to MINOS at RIBF. A. Obertelli thanks the Japanese Society for the Promotion of Science (JSPS) for its support on the last stage of this development.

References

1. C. Detraz *et al.*, Phys. Rev. C **19**, 164 (1979).
2. T. Motobayashi *et al.*, Phys. Lett. B **346**, 9 (1995).
3. B. Bastin *et al.*, Phys. Rev. Lett. **99**, 022503 (2007).
4. A. Gade *et al.*, Phys. Rev. Lett. **99**, 072502 (2007).
5. G. Hagen *et al.*, Phys. Rev. Lett. **109**, 162503 (2012).
6. D. Steppenbeck *et al.*, Nature **502**, 207 (2013).
7. T. Otsuka *et al.*, Phys. Rev. Lett. **105**, 212502 (2010).
8. J. Dobaczewski *et al.*, Phys. Rev. Lett. **72**, 981 (1994).
9. T. Otsuka *et al.*, Phys. Rev. Lett. **87**, 082502 (2001).
10. P. Doornenbal *et al.*, Phys. Rev. Lett. **103**, 032501 (2009).
11. S. Akkoyun *et al.*, Nucl. Instrum. Methods Phys. Res. A **668**, 26 (2011).
12. A. Obertelli, *Proceedings in French-Japanese Symposium on Nuclear Structure Problems*, edited by H. Otsu, T. Motobayashi, P. Roussel-Chomaz, T. Otsuka (World Scientific, 2012).
13. A. Obertelli, T. Uesaka, Eur. Phys. J. A **47**, 105 (2011).
14. C. Demonchy *et al.*, Nucl. Instrum. Methods Phys. Res. A **573**, 145 (2007).
15. C. Demonchy *et al.*, Nucl. Instrum. Methods Phys. Res. A **583**, 341 (2007).
16. S. Agostinelli *et al.*, Nucl. Instrum. Methods Phys. Res. A **506**, 250 (2003).
17. A. Boudard *et al.*, Phys. Rev. C **66**, 044615 (2002).
18. A. Boudard *et al.*, Phys. Rev. C **87**, 014606 (2013).
19. C. Louchart *et al.*, Phys. Rev. C **83**, 011601(R) (2011).
20. L. Audirac *et al.*, Phys. Rev. C **88**, 041602(R) (2013).
21. N.S. Chant, code THREEDEE, University of Maryland, unpublished (1998).
22. D.C. Arogancia *et al.*, Nucl. Instrum. Methods Phys. Res. A **602**, 403 (2009).
23. S.F. Biagi, Nucl. Instrum. Methods Phys. Res. A **241**, 234 (1999).
24. S. Takeuchi *et al.*, in *RIKEN Accelerator Progress Report* (RIKEN, 2005) col. 36, p. 148.
25. T. Kobayashi *et al.*, Nucl. Instrum. Methods Phys. Res. B **317**, 294 (2013).
26. T. Kubo *et al.*, Prog. Theor. Exp. Phys. **2012**, 03C003 (2012).
27. C. Louchart *et al.*, Nucl. Instrum. Methods Phys. Res. A **736**, 81 (2014).
28. A. Gillibert *et al.*, Eur. Phys. J. A **49**, 155 (2013).
29. ASME Boiler and pressure Vessel, `http://go.asme.org/bpvc13`.
30. S.P. Timoshenko, J.M. Gere, *Theory of elastic stability* (Mc. Graw-Hill, 1961).
31. I. Giomataris *et al.*, Nucl. Instrum. Methods Phys. Res. A **376**, 29 (1996).
32. I. Giomataris *et al.*, Nucl. Instrum. Methods Phys. Res. A **560**, 405 (2006).
33. L. Fabbietti *et al.*, Nucl. Instrum. Methods Phys. Res. A **628**, 204 (2011).
34. G. Charpak, I. Giomataris, Ph. Rebourgeard, J.P. Robert, Nucl. Instrum. Methods Phys. Res. A **376**, 29 (1996).
35. P. Colas, I. Giommataris, V. Lepeltier, Nucl. Instrum. Methods Phys. Res. A **534**, 226 (2004).
36. A. Delbart *et al.*, Nucl. Instrum. Methods Phys. Res. A **623**, 105 (2010).
37. N. Abgrall *et al.*, Nucl. Instrum. Methods Phys. Res. A **637**, 25 (2011).
38. CLAS12 Technical Design Report, v5.1, Jefferson Lab (2008).
39. G. Charles, PhD thesis at CEA Saclay, Paris XI university (2013).
40. S. Anvar *et al.*, in *IEEE Nuclear Science Symposium and Medical Imaging Conference (NSS/MIC)* (IEEE, 2011) pp. 745–749.
41. P. Baron *et al.*, IEEE Trans. Nucl. Sci. **55**, 1744 (2008).
42. S. Procureur, Mod. Phys. Lett. A **28**, 1340024 (2013).
43. C. Glattfelder, Mars MX2 User Manual, Enclustra Gmbh (online), available at: `http://www.enclustra.com`.
44. D. Calvet, paper presented at *IEEE NSS/MIC 2013, Seoul, Korea, October 27th-November 2nd 2013.*
45. S. Anvar, in *IEEE Nuclear Science Symposium Conference Record, NSS '08* (IEEE, 2008) pp. 3558–3561.
46. M. Henning, IEEE Internet Comput. **8**, 66 (2004).
47. F. Château, S. Anvar, in *Proceedings of the 15th IEEE-NPSS RealTime Conference, 2007* (IEEE, 2007) pp. 1-6.
48. H. Baba *et al.*, in *IEEE Nuclear Science Symposium Conference Record, NSS '08* (IEEE, 2008) pp. 1384–1386.